2

Seismic Constraints on a Double-Layered Asymmetric Whole-Mantle Plume Beneath Hawai`i

Cheng Cheng[1], Richard M. Allen[1], Rob W. Porritt[1,2], and Maxim D. Ballmer[3,4]

ABSTRACT

It is generally accepted that mantle plumes are responsible for hotspot chains and as such provide insight to mantle convection processes. Among all the hotspots, the Hawaiian chain is a characteristic example that has been extensively explored. However, many questions remain. If a plume does exist beneath the Hawaiian chain, what is the shape, size, and orientation of the plume conduit? To what extent can the seismic structure of the plume be mapped? Can we see a continuous plume conduit extending from the lower to the upper mantle? At what depth do melting processes occur? Here, we combine constraints from three data sets (body waves, ballistic surface waves, and ambient noise) to create 3D images of the velocity structure beneath the Hawaiian Islands from a depth of ~800 km to the surface. We use data from the Hawaiian Plume Lithosphere Undersea Melt Experiment (PLUME), which was a network of four-component broadband ocean bottom seismometers that had a network aperture of ~1000 km. Our multiphase 3D model results indicate there is a large deep-rooted low-velocity anomaly rising from the lower mantle. At transition zone depths the conduit is located to the southeast of Hawai'i. A 2% S-wave anomaly is observed in the core of the plume conduit around 700 km depth, which, once corrected for damping effects, suggests a 200–250°C temperature anomaly assuming a thermal plume. In the upper mantle, there is a horizontal plume "pancake" at shallow depths beneath the oceanic lithosphere, and there is also a second horizontal low-velocity layer in the 250 to 410 km depth range beneath the island chain. This second layer is only revealed after surface wave phase velocity data are incorporated into the inversion scheme to improve the constraints on the structure in the upper ~200 km. We suggest this feature is a deep eclogite pool (DEP), an interpretation consistent with geodynamic modeling [*Ballmer et al.*, 2013]. The model also shows reduced lithospheric velocities compared to the typical ~100 Myr old lithosphere, implying lithospheric rejuvenation by the plume. In addition, a shallow (~20 km) low-velocity anomaly is observed southeast of the Island of Hawai'i. This suggests a newly modified lithosphere, as might be expected in the location of an emerging new island in the Hawaiian chain.

[1]*Department of Earth and Planetary Science, University of California, Berkeley, California, USA*

[2]*Department of Earth Science, University of Southern California, Los Angeles, California, USA*

[3]*Department of Geology and Geophysics, University of Hawai'i at Mānoa, Honolulu, Hawaii, USA*

[4]*Earth-Life Science Institute, Tokyo Institute of Technology, Meguro, Tokyo, Japan*

2.1. INTRODUCTION AND MOTIVATION

The Hawaiian Islands are an ideal place to study intraplate hotspots. Many researchers consider it to be a case example of a deep-rooted whole-mantle plume [*Morgan*, 1971]. While a plume origin is broadly accepted, there is an ongoing debate about the morphology of the plume system, including the depth of origin, and the direction from which the plume originates if it is not vertical. The structure of the plume in the upper mantle and how it interacts with the overriding lithosphere of the

Pacific Plate are also open questions with a variety of geochemical interpretations [e.g., *Lassiter et al.*, 1996; *Abouchami*, 2005; *Huang et al.*, 2011; *Weis et al.*, 2011] and geodynamical models attempting to predict the possible interactions [e.g., *Detrick and Crough*, 1978; *Monnereau et al.*, 1993; *Farnetani and Hofmann*, 2009, 2010; *Farnetani et al.*, 2012; *Rychert et al.*, 2013].

Seismic imaging techniques provide a powerful mechanism to constrain the 3D structure and origin of the island chain. There are several regional seismic studies of Hawai'i that are based on onshore station data [*Woods and Okal*, 1996; *Priestley and Tilmann*, 1999; *Tilmann et al.*, 2001] or offshore station data [*Wolfe et al.*, 2009, 2011; *Laske et al.*, 2007, 2011]. Studies that rely exclusively on on shore recorded data have a limited aperture (width) of the seismic array and the poor ray path coverage makes it impossible to fully assess the deeper mantle structure. More recent regional studies instead make use of the offshore deployment of seismometers during the Plume and Lithosphere Undersea Melt Experiment (PLUME), which increases the aperture and thereby constrains structure over a wider area at shallow depth and also deeper into the lower mantle.

For example, *Wolfe et al.* [2009, 2011] use P- and S-wave arrivals from teleseismic earthquakes to image mantle structure to great depths and conclude that the plume stem extends into the lower mantle, with an origin southeast of Hawai'i. SS precursor observations are consistent with this result [*Schmerr and Garnero*, 2006; *Schmerr et al.*, 2010]. However, imaging with inverse scattering of SS waves has been interpreted to suggest the presence of an 800 to 2000 kilometer wide thermal anomaly in and immediately below the transition zone 1000 km west of Hawai'i [*Cao et al.*, 2011]. The conclusion drawn is that hot material does not rise from the lower mantle through a narrow vertical plume but instead accumulates near the base of the transition zone before being entrained into flow toward Hawai'i. *Cao et al.* [2011] also find a thinned transition zone southeast of Hawai'i but disregard it as the estimated excess temperature is too low and is lower than the 300–400°C estimated excess temperature for the anomaly to the west. *Laske et al.* [2011] analyze Rayleigh waves recorded across the PLUME network at frequencies between 10 and 50 mHz, thereby constraining structure in the upper 100–200 km. Their study reveals lithospheric rejuvenation within an area likely confined to within 150 km of the island chain.

In an effort to better constrain the 3D structure of the upper mantle beneath Hawai'i, we combine body and surface wave observations using a joint inversion scheme [*Obrebski et al.*, 2011] and a finite frequency kernel approach. Our approach uses teleseismic body wave travel time measurements and surface wave phase velocity information from ballistic surface waves and ambient noise cross-correlation measurements. All constraints

are jointly inverted to obtain a multiphase tomographic shear wave velocity model. The resulting model constrains structure from the surface down to ~800 km depth. It is simultaneously consistent with all the seismic observations, meaning that it takes advantage of the surface wave constraints to resolve shallow (<200 km) structure, while being consistent with teleseismic travel-times that are able to constrain deeper structure.

2.2. DATA AND METHOD

The PLUME experiment included a large network of four-component broadband ocean bottom seismometers (OBSs) occupying more than 70 sites and having an overall aperture of more than 1000 km [*Laske et al.*, 2009]. PLUME was designed as a tool to determine the deep-mantle seismic velocity structure beneath the Hawaiian hotspot island chain. PLUME was a two-year deployment that ran from January 2005 through June 2007. The first stage of this deployment was a 500 km wide OBS network with interstation spacing of ~80 km, where data were recorded continuously from January 2005 through January 2006. In the second stage of the deployment, the OBSs occupied a 1000 km wide region with station spacing of about 220 km from April 2006 through June 2007. In this two-phase deployment, data from the broadband sensors had undetermined orientations.

The first step in our processing is orienting the PLUME OBS horizontal components using teleseismic P-wave particle motions. Generally, our method produces stable and reliable orientations (average standard deviation is about 6°) over a wide range of earthquake back azimuths. To maximize the signal-to-noise ratio (SNR), we began by applying a 0.04–0.1 Hz bandpass filter and measured ~1100 P-wave relative arrival times on vertical component data. These P-wave measurements were used to determine orientations. We compared our estimated orientations with those determined using surface waves and found them to be consistent. Once these data were rotated to radial and transverse orientations, ~750 S-wave relative arrival times (including direct S and SKS phases) were determined from the SV component via multi channel cross correlation. Of these, we selected 75 events distributed in as wide a range of back azimuth directions as possible (Figure 2.1), restricting the data to events with epicentral distances greater than 30° and M_w >5.5. As part of the waveform-by-waveform quality control, arrivals were picked manually using the Antelope dbpick software. This software has an interface for viewing waveform data and the ability to pick arrival times and provides markers that are then used as a starting point for the cross-correlation step. We use a multi channel least squares cross-correlation approach [*VanDecar and Crosson*, 1990] that results in a relative travel time delay data set. We select only the highest quality data based on
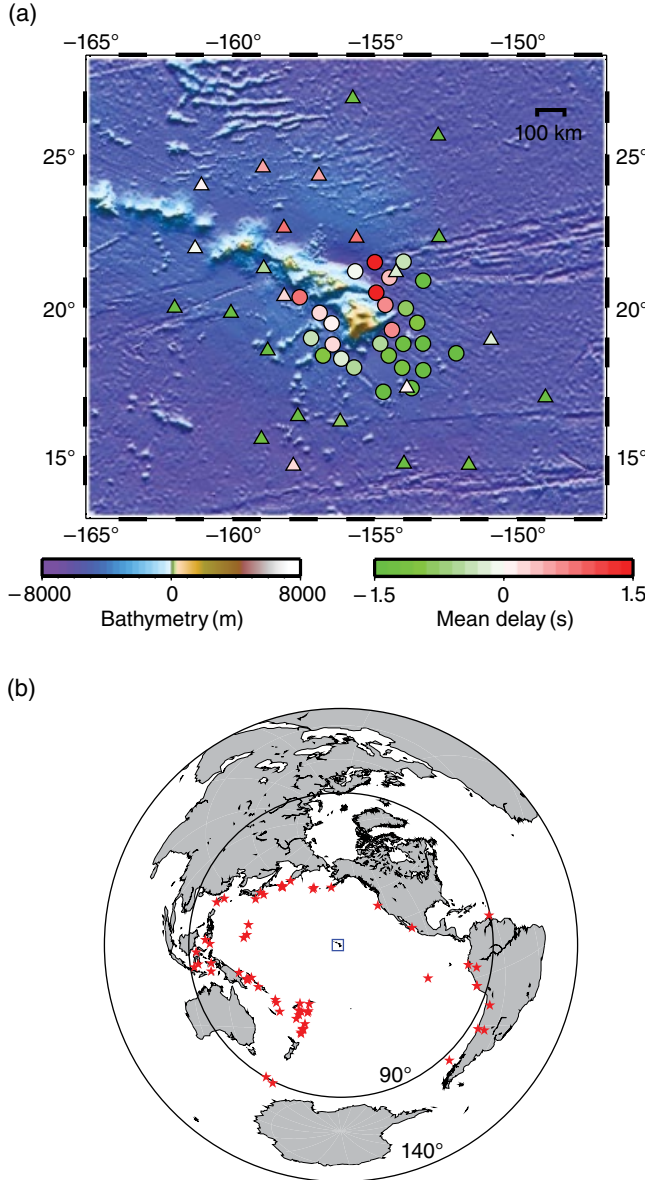
(a)

(b)

Figure 2.1 Map of the study area. (a) Ocean bathymetry showing seismometer locations. Stations deployed in the first year are indicated by circles and those deployed in the second year are marked by triangles. The station colors indicate the mean body wave delays (measured at 0.04–0.1 Hz). Only stations that successfully recorded data are shown. (b) Map of earthquakes (red stars) used in this study and our study location (blue box). Black circles are 90° and 140° from the study region.

the standard deviation of the cross-correlation-derived delay times to make sure that our body wave data set contains reliable shear arrivals [*Obrebski et al.*, 2011].

The surface wave phase data we use here come from two different sources. The first is ambient noise cross-correlation measurements in the period band of 10–25. Due to the relatively high noise environment of OBS data, a linear stack of ~1 year of ambient noise empirical Green's function results is still rather noisy, which

makes accurate measurements of surface wave phase velocity difficult. To reduce this problem, we apply a time-frequency domain phase weighted stacking (tf-PWS) method [*Schimmel and Gallart*, 2007; *Schimmel et al.*, 2011], which efficiently increases the SNR. The tf-PWS is an extension of the phase-weighted stack method that is a non linear stack where each sample of a linear stack is weighted by an amplitude-unbiased coherence measure. The idea here is leveraging the time-frequency phase stack, which is based on the time-frequency decomposition of each trace obtained through the S transform. The results before and after applying the tf-PWS differ significantly (Figure 2.2) and the number of visible dispersion curves within each period band after implementing the tf-PWS is greatly increased. From our time-frequency analysis we observe two wave trends with different travel times (Figure 2.2). The T1 phase is the surface wave energy and the T2 phase is the acoustic wave propagating in the water.

The second source of phase velocity measurements comes from ballistic surface waves. These are the direct surface wave energy as opposed to scattered energy, including ambient noise. We use a two-plane wave tomography method [*Forsyth and Li,* 2005; *Yang and Forsyth,* 2006a, 2006b] in the period band of 25–100. Different from the traditional two-station one-plane-wave method, our method uses the amplitude and phase information simultaneously and the interference of two plane waves to model each incoming teleseismic wavefield. This approach can account for the scattering and multipathing caused by lateral heterogeneities and was developed to image regional-scale structures with network apertures typically up to 1000 km, for example, PLUME. This method has been applied successfully in various regions with a similar network configuration as ours [e.g., *Yang and Forsyth,* 2006b; *Yang et al.*, 2008]. Using the same methodology, we derive phase velocity at a variety of period bands from 25 to 100 s.

To simultaneously invert the phase velocity constraints with the body wave relative travel time constraints, we must determine phase velocity anomaly constraints. This is achieved by subtracting the phase velocities calculated for a background model from the absolute phase velocities. We explored the use of several background models and compared the resulting velocity structure at different crustal depths. We found only slight differences in the models indicating that the choice of background model used does not significantly alter our results. Given this, we used the global average ocean Preliminary Reference Earth Model (PREM) model as the background model.

Following *Obrebski et al.* [2011] we create a joint matrix of body wave relative travel time anomalies and the surface wave phase velocity anomalies to use in a joint inversion. The model space extends from 165°W to 145°W and 12°N to 28°N and to a depth of 1000 km. The model grid
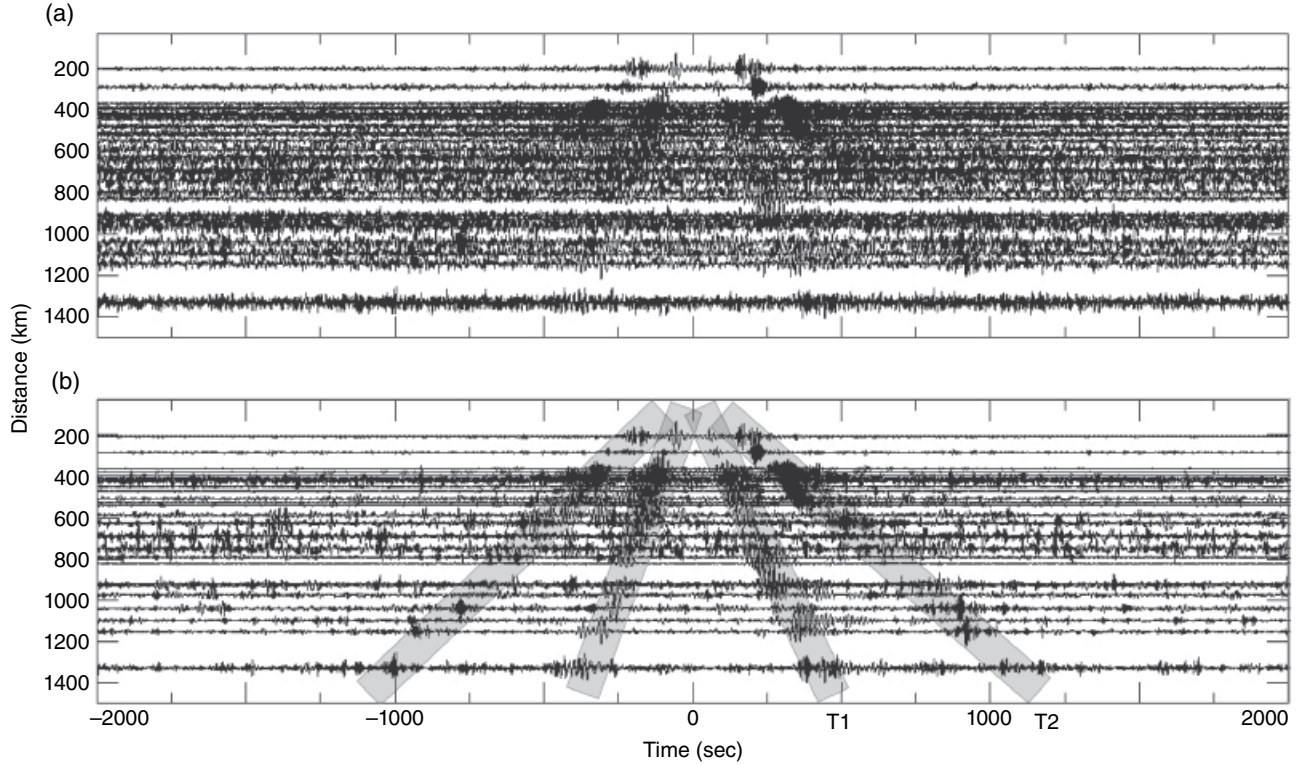
(a)

(b)

Figure 2.2 Seismic record sections. (a) Record section of the ambient noise cross-correlation between station PL41 and other stations derived using a traditional linear stacking method. (b) The record section shown in (a) except derived using a phase-weighted stacking method [*Schimmel and Gallart*, 2007; *Schimmel et al.*, 2011]. Boxed phases, labeled T1 and T2, are surface waves and acoustic waves propagating in the water column, respectively.

includes 33 nodes in both the horizontal and vertical directions, yielding grid spacings of ~30 and ~55 km in the vertical and horizontal directions, respectively. The relative body wave delays are inverted using finite-frequency sensitivity kernels that account for the frequency-dependent width of the region to which body waves are sensitive and also accounts for wavefront healing effects. Our tomographic method uses paraxial kernel theory to calculate the Born approximation forward scattering sensitivity kernels for teleseismic arrival times [*Dahlen et al.*, 2000; *Hung et al.*, 2000, 2004]. The surface wave matrix is made of relative phase velocities estimated for 15 frequencies (10, 12, 15, 18, 20, 22, and 24 s, contributed from ambient noise; 25, 29, 33, 40, 50, 66, 83, and 100 s, contributed from ballistic surface waves) at each node, which constrain the velocity structure from 0 to 300 km depth. To weight the body wave and surface wave constraints in the joint matrix, we use the same weighting scheme as *Julia et al*. [2000] and *Obrebski et al*. [2011]. They define the parameter p in their weighting formula, which allows for a manual tuning of the relative contribution of each data set. After experimentation with various values of p, we settled on using a value of 0.7 as optimal. The sensitivity of very shallow (<60 km) velocity structure to the body waves is also reduced through a ramp parameter. This is set to zero at the surface and increases

linearly to 1 at 60 km depth. This is a multiplicative factor applied to the body wave kernels to prevent the body waves from introducing very short wavelength (one station spacing) velocity anomalies at shallow depths where the ray paths are vertical and there is no resolution. The shallowest part of our model is therefore entirely determined by surface wave data constraints. Station terms and event corrections are also included in the inversion. Our inversion requires damping and uses least-squares QR (LSQR) [*Paige and Saunders*, 1982] to iterate to a final model. We also apply a smoothing factor to the model space. To choose the inversion damping parameter, we examine the residual misfit curves as a function of the model norm and find 0.2 is the best damping factor for our inversion scheme.

2.3. IMAGING RESULTS

As a first reference model we produce a smoothed 3D model derived using inversion of only the SV body wave travel times, which we refer to as HW13-SV (Figures 2.3, 2.4b, and 2.4e). The structure is very similar to the teleseismic body wave result of *Wolfe et al*. [2009], as we would expect. We observe a fairly continuous low-velocity feature extending from the surface down through the transition zone and into the deep mantle (Figures 2.3 and 2.4b). We
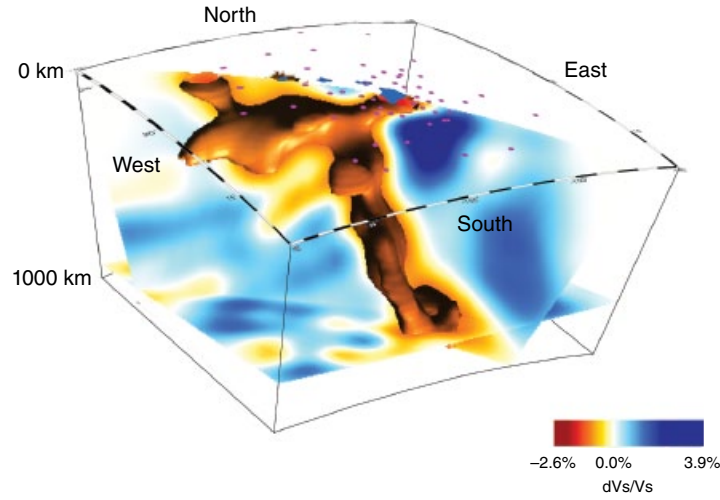
Figure 2.3 A 3D view of our body-wave-only S-wave velocity anomaly model (HW13-SV) for the mantle beneath Hawai'i. Warm colors indicate low-velocity anomaly and cool colors indicate high-velocity anomaly. The value of the isosurface is –1.5%. The model reveals a low-velocity region elongated in the sub vertical direction from the base of the model extending up into the uppermost mantle. This feature is several-hundred kilometers wide and dips to the southeast. We interpret it as the plume conduit. In the upper mantle the low-velocity anomalies are predominantly horizontal and oriented parallel to the island chain. We interpret this as the plume "head," i.e., material that is being dragged along with and beneath the Pacific lithosphere.
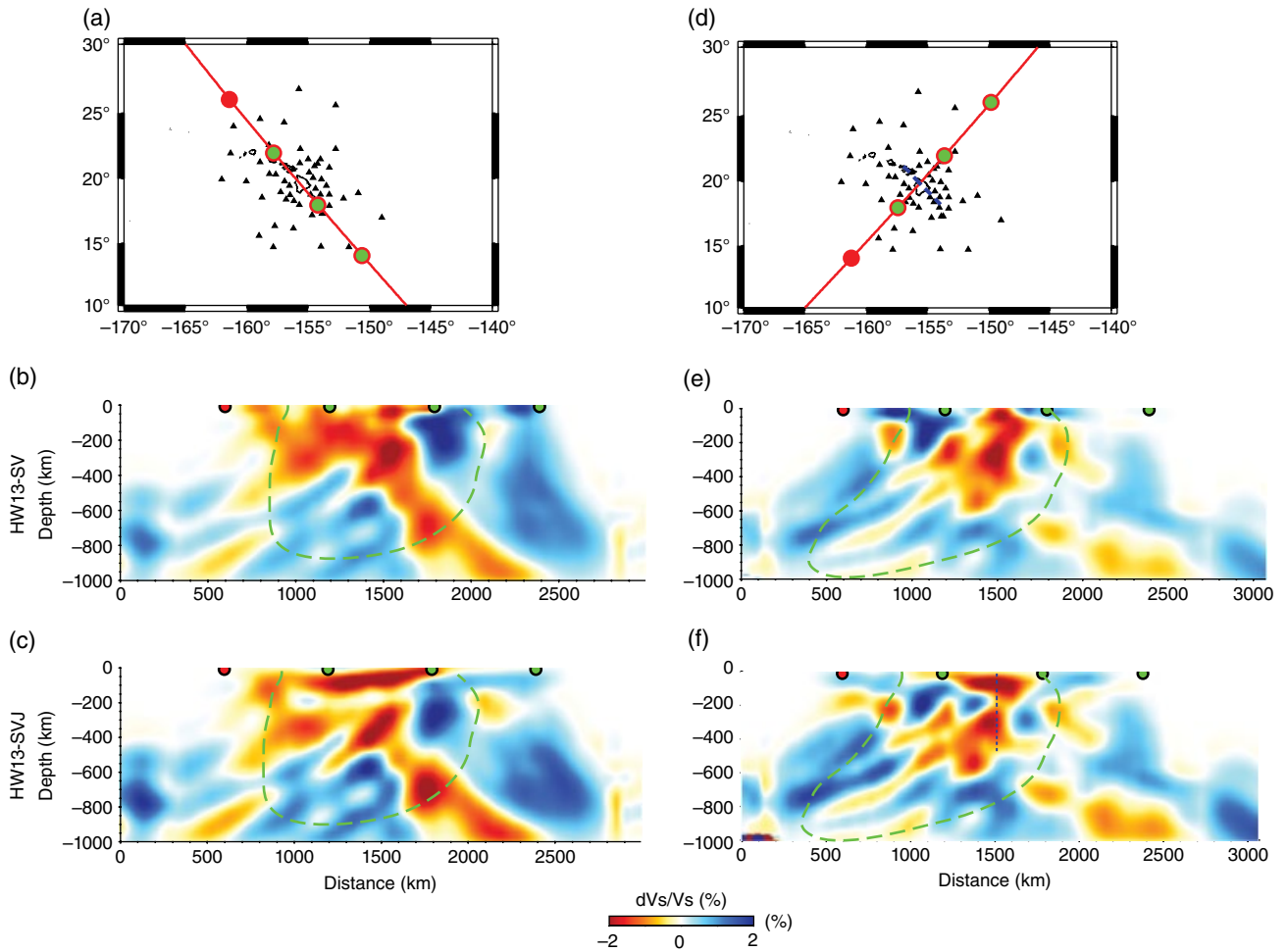

Figure 2.4 Vertical cross sections through the HW13 models: (b, c) cross sections parallel to the Pacific Plate motion; (e, f) cross sections perpendicular to the plate motion. The locations and orientation of the cross sections along with the distribution of stations are shown in (a,d). Results (b) and (e) are from the body-wave-only inversion (HW13-SV); (c) and (f) are from the joint ambient noise, surface wave and body wave inversion (HW13-SVJ). The dashed green contours encompass areas with highest teleseismic body wave ray coverage. The vertical dashed blue line in (d) is beneath the center of the island chain.
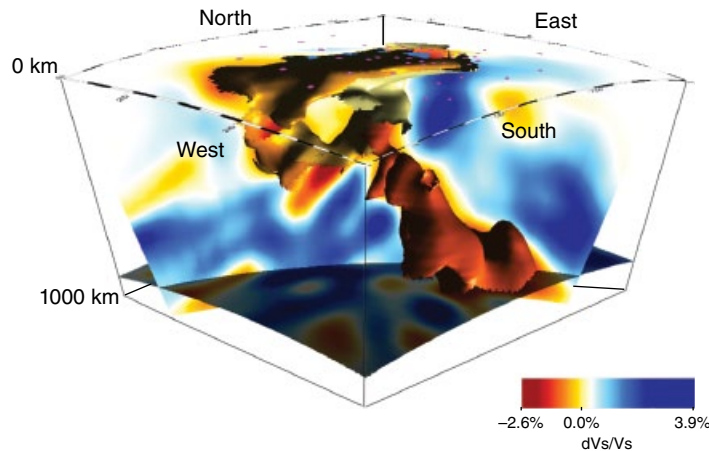
Figure 2.5 A 3D view of our body wave and surface wave joint S-wave velocity anomaly model (HW13-SVJ). This is shown with a similar perspective to the 3D image of HW13-SV in Figure 2.3. The model shows what is interpreted as the plume conduit extending from the lower mantle southeast of Hawaiʻi up into the upper mantle beneath Hawaiʻi. In the upper mantle two subhorizontal plume pancakes are observed. The shallow pancake is clearest and extends beneath the lithosphere to a depth of 150 km. The second pancake is less continuous but forms a subhorizontal layer in the 250–400 km depth range. We interpret this as the DEP. This feature is revealed in the joint inversion due to the improved resolution in the upper mantle.

interpret this as a plume conduit, the main stem of which comes from the mantle to the southeast of the surface islands. In the upper mantle, low velocities are observed over a wider region extending the length of the island chain and from the surface down to ~400 km depth. We interpret this low-velocity body as the present-day plume "pancake," i.e., the low-velocity material that is spreading horizontally beneath the oceanic lithosphere. What is surprising about this image is the fact that the low velocities of the plume pancake extend so deep, an observation also noted by *Wolfe et al.* [2009]. Both geodynamical models and previous tomographic observations of mantle plumes in oceanic settings suggest a much thinner sublithospheric plume pancake confined to the upper ~250 km [*Ribe and Christensen*, 1994; *Allen et al.*, 2002; *Farnetani and Hofmann*, 2010].

In an effort to better resolve this unusual structure in the upper mantle, we complete the joint inversion of body and surface wave constraints, which we refer to as HW13-SVJ (Figures 2.4c, 2.4f, 2.5, and 2.6). This model retrieves a more complex velocity structure in the upper mantle than HW13-SV (Figures 2.3, 2.4b, and 2.4c), as would be expected given the additional constraints. The upper mantle low-velocity feature is now observed to separate into two sub horizontal layers. The first is shallow and immediately beneath the oceanic lithosphere and extends to ~150 km depth. The depth extent is clearest in Figure 2.4c and its lateral extent beneath and along the island chain is shown in Figure 2.6b. The second layer is in the depth range of ~250–400 km and is somewhat less continuous in the horizontal direction than the shallow layer (Figures 2.4c, 2.5, and 2.6d), but is distinct from and not continuous with the shallow layer, as illustrated by the

absence of significant low velocities at 200 km depth (Figure 2.6c). This deeper low-velocity anomaly is less continuous beneath the island chain than the shallow anomaly (compare Figures 2.6b and 2.6d). Finally, our seismic model also shows an apparent asymmetry in the low-velocity structure of this second layer, which may be related to geochemical differences between the Loa and Kea trends observed at the surface [*Huang et al.*, 2011; *Weis et al.*, 2011] (see also Chapter 3).

We also invert for absolute velocity using just the (ambient and ballistic) surface wave data in order to compare these absolute velocities with average Pacific velocity profiles. Absolute velocity profiles at three locations along the island chain are shown in Figure 2.7. These profiles show that southeast of the island, out in front of the region of plume influence, the velocity structure is typical for the 100 Ma lithosphere below ~75 km depth. Beneath the islands we see evidence of a rejuvenated velocity profile. One inconsistency with previous surface-wave-based studies is the fact that we do not see the peak of the low-velocity anomaly around 100 km depth centered west of the Island of Hawaiʻi, as suggested by *Laske et al.* [2011]. Instead, the velocity anomalies we image at these depths are aligned with and centered on the island chain, which is consistent with crustal studies of the underplating process [*Leahy et al.*, 2010], body wave tomography [*Wolfe et al.*, 2009, 2011], and the geometry and geoid anomaly of the Hawaiian Swell [*Cadio et al.*, 2012]. We do see the low-velocity anomalies extending further to the west than to the east, which is consistent with a recent receiver function study suggesting that the melt path to the Island of Hawaiʻi originates to the west [*Rychert et al.*, 2013].
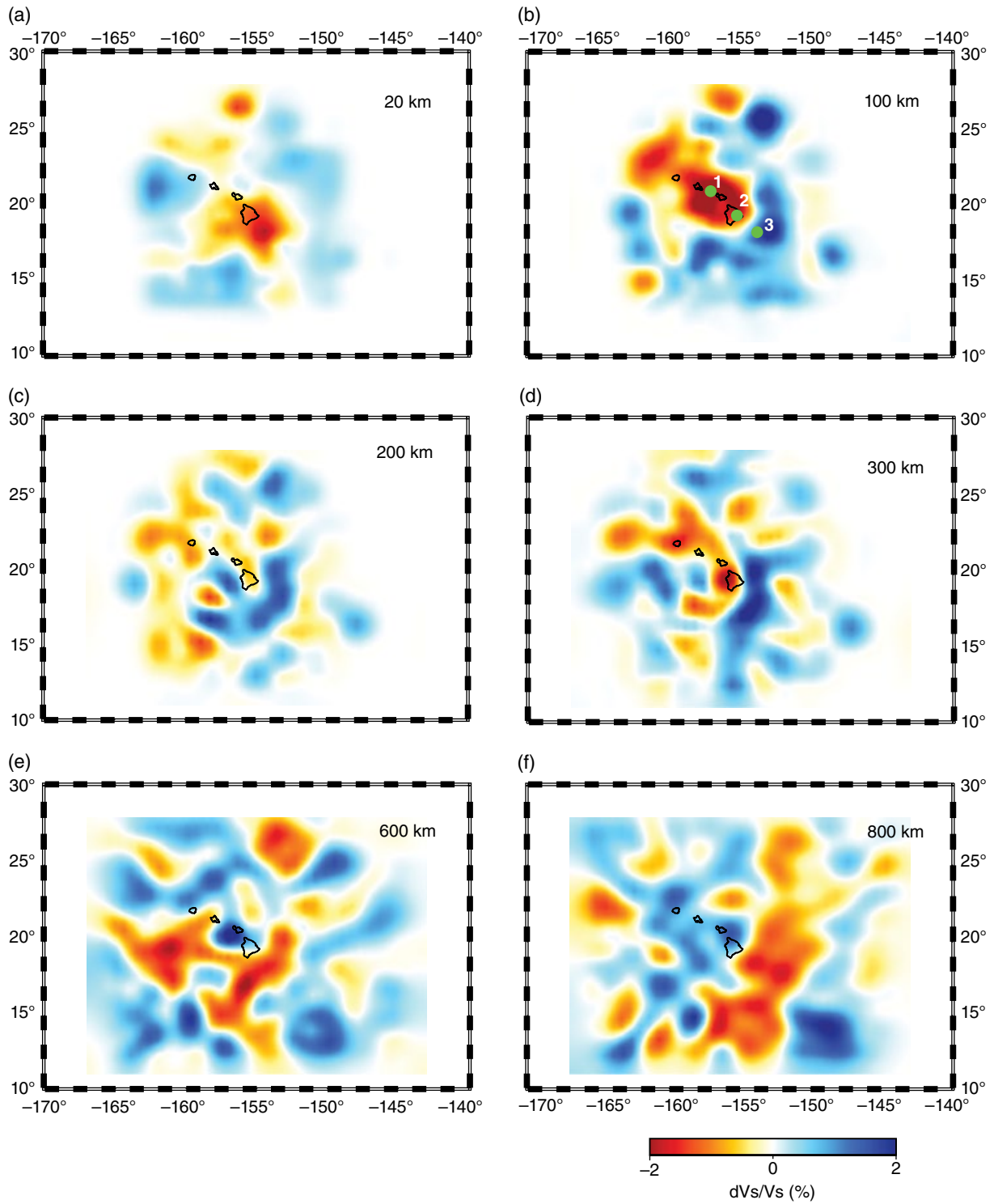
Figure 2.6 Maps of shear wave velocity perturbations in HW13-SVJ at (a) 20, (b) 100, (c) 200, (d) 300, (e) 600 and (f) 800 km depth. Numbered green dots in subpanel (b) are the locations of low-velocity zone 1, low-velocity zone 2, and high-velocity zone 3 in Figure 2.7.
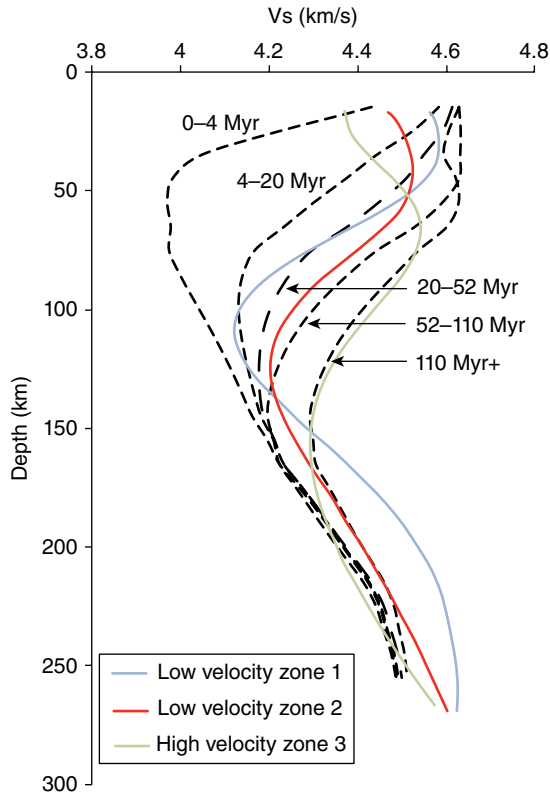
Figure 2.7 Upper mantle absolute velocity profile derived from ambient noise and surface wave inversions. The dashed lines are average mantle velocity profiles for the Pacific lithosphere with various ages [*Nishimura and Forsyth*, 1989]. The colored lines show the velocity profiles at various locations along the length of the island chain and are indicated in Figure 2.6b.

Figure 2.8 Vertical cross section of ray density maps. (a) Cross section that is parallel to the Pacific Plate motion where the dashed green line encompasses areas with "high" ray coverage. This cross section is the same as shown in Figures 2.5b and 2.5c. The color bar shows how many rays contributed to the velocity information at a particular model grid point. (b) Cross section perpendicular to the Pacific Plate motion and the same as shown in Figures 2.5e and 2.5f.

2.4. RESOLUTION

We explored the resolving capabilities of our models using several approaches. First, we show the ray density from the teleseismic body wave data set. Figure 2.8 shows the region with highest ray density plotted in the same cross sections as the model shown in Figure 2.4. The coverage is densest immediately beneath the seismic network and to a depth similar to the maximum aperture of the network. The green dashed line outlines the region of dense coverage and is also plotted on the model in Figure 2.4. Ray density is by no means a complete indicator of resolution (see the following additional tests) and crossing rays are needed to resolve structure. However, it is an indicator of where there are many ray paths constraining the velocity structure.

We next conduct checkerboard resolution tests using synthetic velocity models consisting of alternating high- and low-velocity boxes. These synthetic velocity models are used to generate synthetic data, that are then inverted to assess the ability of the data set to recover the synthetic models. Again, these types of tests are not perfect and do make the assumption that the finite frequency sensitivity
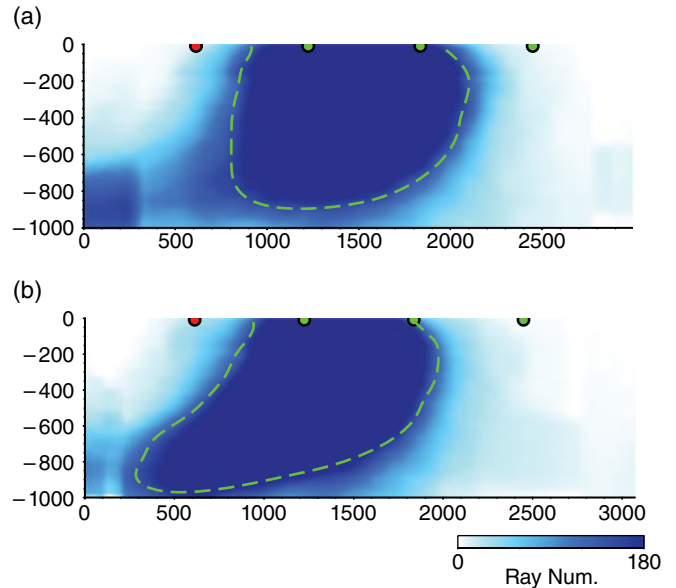
kernels used are a "perfect" representation of the true sensitivity of the constraints. We do add 5% noise to the constraints to simulate errors and uncertainties in the measurements made. The recovered velocity models provide a guide to how the scale of structure that can be resolved varies as a function of position in the model. Resolution is possible on shorter scales at shallow depths, primarily due to the inclusion of surface waves, and structures must be larger to be constrained at greater depths. Figure 2.9 shows that velocity anomalies ~200 km in diameter can be imaged in the upper ~250 km where surface waves provide constraints. At depths where the teleseismic body waves provide most constraint, i.e., from ~300 to ~600 km, structures ~350 km wide are well recovered. Finally, in the uppermost lower mantle only structures ~450 km wide are recovered.

Finally, we construct a suite of synthetic velocity models to further test the ability of our data set to resolve a variety of input velocity structures. We focus on the ability of the data set to constrain vertical plumelike anomalies at a variety of depths. Figure 2.10 shows the input and the recovered velocity structure for tests with a vertically oriented low-velocity anomaly 200 km wide and with a peak velocity anomaly of −4%. In the first test (Figures 2.10a, and 2.10e) the anomaly extends from 0 to 300 km. The recovered velocity structure successfully captures the input structure in that the strongest low-velocity
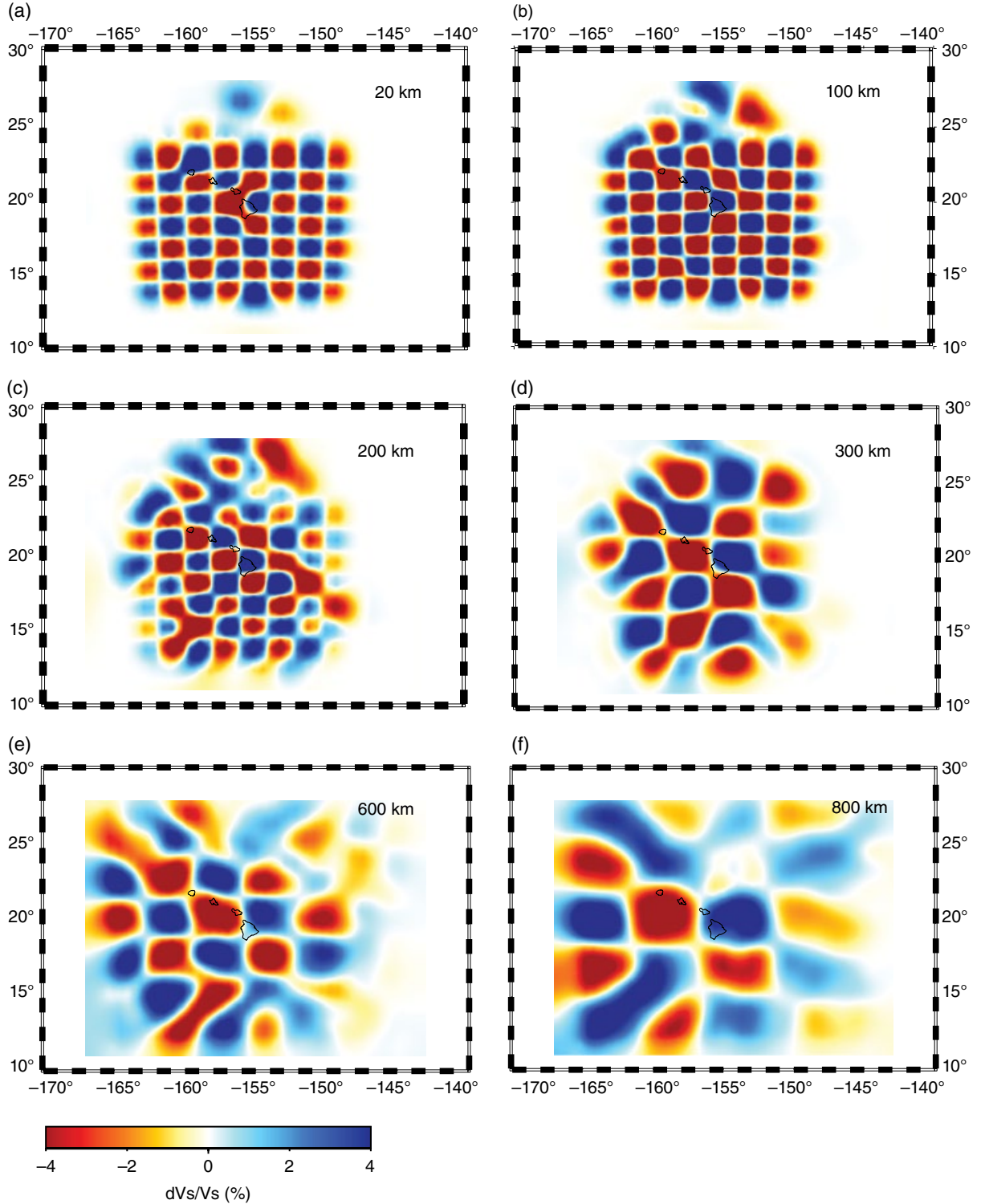
Figure 2.9 Checkerboard resolution tests for input (synthetic) velocities anomalies of ±4%. Horizontal slices through the recovered velocity anomalies are shown at depths of 20, 100, 200, 300, 600, and 800 km.

anomaly also extends from 0 to 300 km depth and has approximately the same width. The amplitude of the anomaly also approaches the input −4% at most depths. Ray path smearing effects are also seen with high- and low-velocity anomalies radiating down and outward from the input velocity structure. However, these smearing effects are all low amplitude with the largest streaking anomalies only being ~0.5%. Based on this test, we
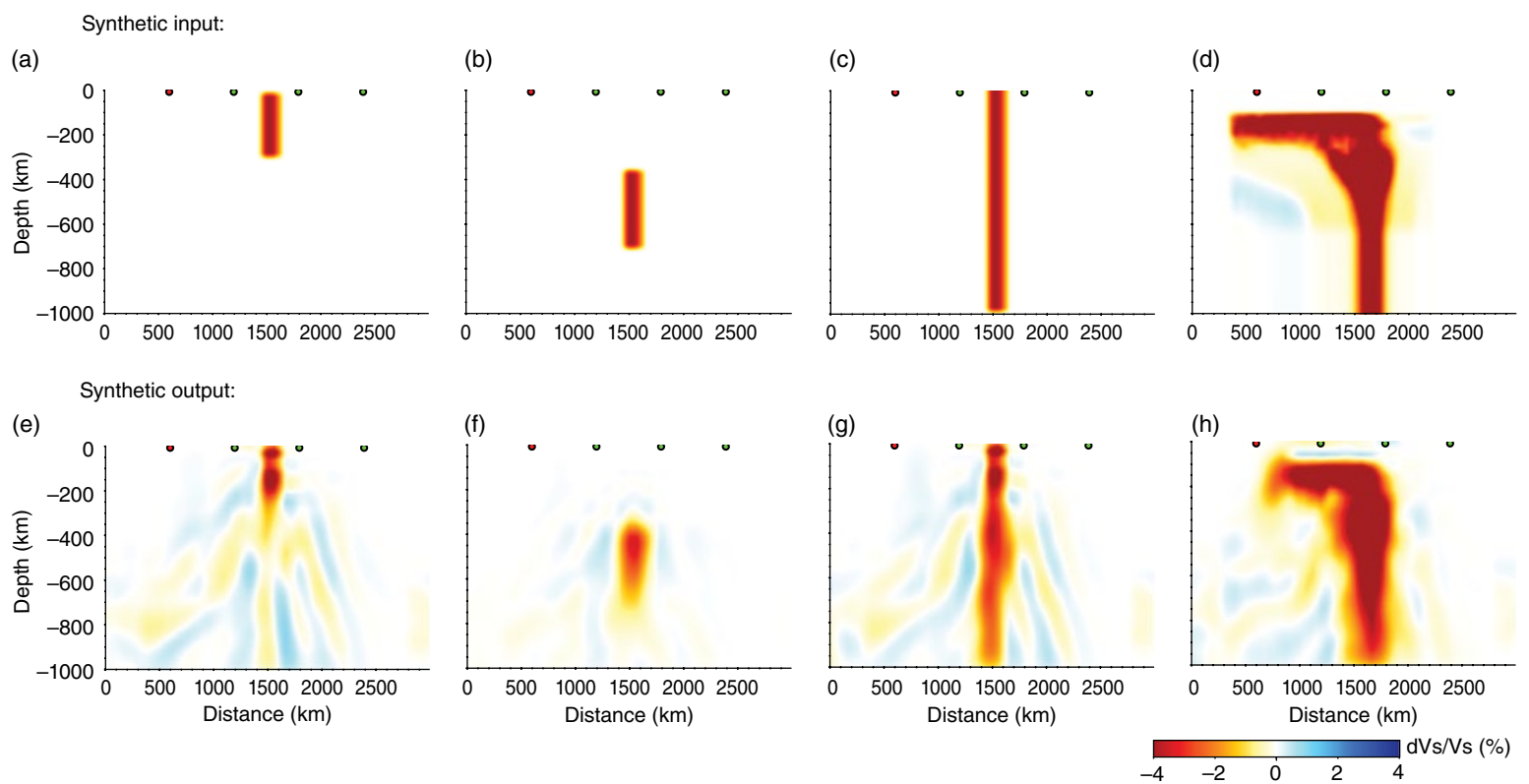
Synthetic input:

Figure 2.10 Synthetic resolution tests: (a–d) vertical cross sections through four synthetic input velocity models; (e–h) recovered velocity structure. These tests include vertical columns in various depth ranges (a–c; e–g) and a test of the model structure expected for *Ballmer et al.'s* [2013] geodynamic model (d, h). The sections are all parallel to plate motion as in Figures 2.4b, 2.4c, and 2.8a.

conclude that our model would show a strong velocity anomaly constrained to the upper 300 km if the true anomaly structure was only in the upper 300 km. Next we explore the possibility that the low-velocity anomaly is only 350–650 km deep (Figures 2.10b and 2.10f). Again the recovered velocity structure is largely constrained to the same depth range with less smearing than the first test. The amplitude recovery is reduced to −2% to −3%, meaning that we only recover 50%–75% of the velocity anomaly. Next we use a low-velocity anomaly that extends throughout the full depth range of the model (Figures 2.10c and 2.10g) and find that this is also well recovered with only low-amplitude anomalies resulting from smearing of velocities along downward going ray paths similar to what was observed in the first test. The amplitude of the velocity anomalies in the input plume stem also decreases with depth in a similar fashion to the first two tests.

In the final test we use a synthetic velocity structure based on the "two-layer" geodynamic model for mantle flow beneath Hawai'i developed by *Ballmer et al*. [2013]. We estimated the absolute velocities from the predicted temperature, density, and lithostatic pressure at each point of the quasi-steady-state model using the relationships of *Faul and Jackson* [2005] and *Jackson and Faul* [2010] with specifications reported in *Ballmer et al*. [2013]. We then subtract the 1D reference velocity model to determine velocity anomalies for input into our synthetic test. The recovered structure is good beneath the seismic array, including the variable size of the low-velocity anomaly in the upper mantle associated with Ballmer's two-layer structure. These tests leave us confident that the upper mantle structure is well resolved in our seismic inversion.

2.5. DISCUSSION

2.5.1. Structure and Origin of Plume Conduit

Our imaging results suggest that a subvertically oriented low-velocity anomaly exists beneath Hawai'i that extends through the upper mantle and down into the uppermost lower mantle. We interpret this feature as being indicative of a whole-mantle-plume source for the Hawaiian island chain. This structure and interpretation is similar to the conclusion of *Wolfe et al*. [2009]. Both results reveal low velocities within the mantle transition zone and in the topmost lower mantle, suggesting there is a deep source region for the Hawaiian plume. A thermal boundary layer near the base of the transition zone has been suggested as a candidate source region for some plumes [e.g., *Cserepes and Yuen*, 2000]. However, our image does not support this hypothesis as we see no evidence of a broadening of the low-velocity anomaly beneath the 660 km discontinuity, as would be expected in that case.

We interpret our model to indicate that the plume conduit has an origin southeast of the Island of Hawai'i. As shown by Figures 2.4 and 2.6, there are several locations in the uppermost lower mantle that have low velocities in our model. However, we interpret the anomaly to the southeast to be the plume conduit for three reasons. (1) The low velocities in the southeast quadrant are larger in size (lateral extent) and amplitude (see Figure 2.6f) than any other quadrant, reaching 2% when others are closer to 1%. (2) The smaller low-velocity anomalies seen in other quadrants are outside the region of dense ray coverage, i.e. outside the green dashed lines in Figure 2.4. (3) The anomalies extending southeast are the most continuous (Figures 2.4 and 2.5). It is also worth noting that the teleseismic ray coverage is not dominated by rays coming from the southeast (Figure 2.1b) so the plume conduit that we image/interpret is not due to a particularly dense ray bundle coming from that direction. Our observation that the plume origin is to the southeast is also consistent with geodynamic arguments that mantle convection in general, and the fast-moving Pacific Plate in particular, shear and tilt the plume conduit in the upper and lower mantle [*Richards and Griffiths*, 1988; *Steinberger and O'Connell*, 1998; *Steinberger et al*., 2004; *Farnetani and Hofmann*, 2010].

Several previous studies have explored topography of the transition zone discontinuities in the region beneath Hawai'i in an effort to identify anomalies that may be related to the source of the islands. *Shen et al*. [2003] observe transition zone thinning across a broad zone beneath the island chain, which they interpreted as reflecting higher-than-normal temperatures beneath the region due to the passage of plume material through the transition zone. In contrast, *Li et al*. [2000] and *Wölbern et al*. [2006] suggest that the transition zone is thinned ~200 km west of Hawai'i. In a study of SS precursors, *Cao et al*. [2011] argue that ponded plume material sits beneath the transition zone several degrees west of Hawai'i. Our imaging results do not support these observations, instead suggesting that the plume conduit is intersecting the transition zone ~200 km southeast of Hawai'i.

A number of factors can cause velocity heterogeneity in the mantle, including variations in temperature (with contributions from both anharmonic and anelastic components [e.g., *Karato*, 1993]), water content [*Karato*, 2003], melt [e.g., *Hammond and Humphreys*, 2000], grain size [*Faul and Jackson*, 2005; *Jackson and Faul*, 2010], and bulk composition. The last factor includes depletion by melt extraction [*Jordan*, 1979], although recent studies suggest that the effects of depletion on P- and S-wave velocities and V_p/V_s ratios may be minor [*Schutt and Lesher*, 2006; *Afonso et al*., 2010]. In the uppermost lower mantle (~700 km depth) the S wave velocity anomalies are around 2% in our model. As smoothing and damping are

part of the inversion scheme, the velocity anomalies we obtain are minimum estimates [*Allen et al.*, 2002]. From our synthetic tests (Figure 2.10) we find that we recover about 50%–75% of the anomaly at this depth, which implies the real velocity anomalies in the plume conduit likely exceed ~3% [*Allen and Tromp*, 2005]. These velocity anomalies imply an excess temperature of 200–250°C [*Schilling*, 1991; *Allen et al.*, 2002], consistent with petrological estimates [*Herzberg et al.*, 2007].

2.5.2. Upper Mantle Structure and Double-Layered Plume

The low-velocity structure that we image in the upper mantle is in disagreement with the classic version of plume theory. The classic plume model [e.g., *Morgan*, 1972; *Ribe and Christensen*, 1994; *Farnetani and Hofmann*, 2010] involves a near-vertical plume conduit rising through the entire mantle and spreading at the base of the lithosphere to form a pancake of hot material. The main hotspot forms where the conduit feeds the pancake, which is dragged away by plate motion, to the northwest in the case of Hawai'i. However, instead of a single shallow plume pancake, we image two distinct horizontal low-velocity layers in the upper mantle. One layer is at <150 km depth, and the second is in the ~250–400 km depth range. Whereas this study is the first to image two separate layers, it is consistent with a previous study from *Wolfe et al.* [2009], who have recovered one broad low-velocity body that extends from the base of the lithosphere to ~400 km depth.

Our imaged model structure is consistent with a recent geodynamic model [*Ballmer et al.*, 2013] developed in an effort to explain the thick low-velocity body imaged by *Wolfe et al.* [2009]. While the model was developed simply to explain the existence of a plume pancake to ~400 km depth beneath the island chain, it also suggests a double layer to the plume pancake, as we observe. In Ballmer et al.'s model the plume is composed of 85% peridotite and 15% chemically dense eclogite. As the plume material rises through the upper mantle, it generates a deep eclogitic pool (DEP) at 300–410 km depth, from which a shallow upwelling rises further to feed the pancake [*Ballmer et al.*, 2013]. The compositions used in the geodynamic model are based on geochemical constraints for Hawaiian lava composition, which is thought to contain mafic materials such as eclogites, in addition to peridotite [*Hauri et al.*, 1996; *Sobolev et al.*, 2005; *Herzberg*, 2011; *Pietruszka et al.*, 2013]. These mafic materials likely originate from subducted oceanic crust that is entrained by the plume and are denser than peridotite throughout the upper mantle. The ascent of a plume rich in eclogite is thus controlled by a competition between negative compositional and positive thermal buoyancy. In addition, it is affected by phase transitions in the upper mantle that modulate the densities of eclogite and peridotite to cause a maximum of the excess density of eclogite at 300–410 km depth [*Aoki and Takahashi*, 2004]. It is this excess density maximum that causes the plume to stall and to form a DEP [*Ballmer et al.*, 2013]. When the material rising out of the DEP crosses the coesite-stishovite phase transition at 300 km depth [*Aoki and Takahashi*, 2004], the density of eclogite sharply decreases, thereby inducing rapid upwelling in a narrow plume conduit. The predicted contrast between a wide DEP and a narrow shallow plume [*Ballmer et al.*, 2013] compares well with our observations (Figures 2.5 and 2.6).

2.5.3. Plume Interaction with Lithosphere

The age of the Pacific Plate around the Hawaiian Islands is about 100 Ma [*Müller et al.*, 2008]. Figure 2.7 shows the typical velocity profiles for oceanic plates of different ages derived from surface wave measurements [*Nishimura and Forsyth*, 1989]. We determine the absolute velocity based on our surface wave constraints and compare them to the typical profiles at three different locations that span regions in both the low- and high-velocity portions of the lithosphere (green dots in Figure 2.6b). Location 1 is halfway along the island chain, which is in the middle of the strong low-velocity anomaly at ~100 km depth. Location 2 is at the southwest coast of the Island of Hawai'i and on the edge of the strong low-velocity anomaly. Location 3 is further southwest and "upstream" of the plume, outside the low-velocity region of the plume.

Compared to the typical 100 Ma lithosphere velocity profile that would be expected beneath Hawai'i, the velocity at location 1 is most reduced. The velocity reduction extends from the surface to ~140 km, producing a velocity profile that is more similar to the typical profile for the 20–52 Ma lithosphere. The velocity at location 2 is also reduced to ~140 km depth, but to a lesser extent. These observations are consistent with the concept of lithospheric rejuvenation [e.g., *Detrick and Crough* 1978; *Von Herzen et al.*, 1989; *Monnereau et al.*, 1993; *Li et al.*, 2004]. Location 1 has been rejuvenated to a greater extent than location 2, as would be expected given that location 1 has been under the influence of the lithosphere-modifying plume for a longer time than location 2. Our observations are consistent with those of *Laske et al.* [2011]. We suggest rejuvenation of the lithosphere should be understood primarily as a velocity reduction in the lithosphere and not necessarily a mechanical thinning of the lithosphere.

Location 3 is 150 km southeast of the Island of Hawai'i and is upstream of the plume. We therefore expect little or no rejuvenation effect. Below 75 km depth the velocity profile at location 3 is very similar to the typical profile for the 100 Ma lithosphere (Figure 2.7). However, the velocity is
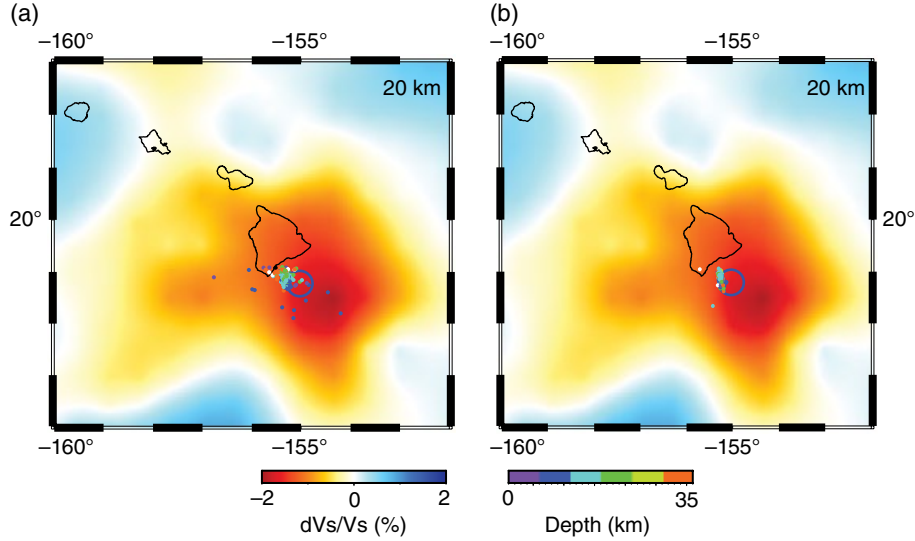
Figure 2.11 Map view of HW13-SVJ at 20 km depth with the location of earthquake swarms from (a) 1971 and (b) 1996 and the location of the Lōʻihi Seamount (blue circle). The lower right color scale indicates earthquake depth and the lower left color scale indicates velocity perturbation in percent.

significantly reduced at shallower depths. The shallow low-velocity zone is also imaged in HW13-SVJ (Figures 2.6a and 2.11). We are able to image this low-velocity anomaly at 20 km depth due to the inclusion of the higher-frequency constraints from ambient seismic noise (down to 0.1 Hz), which have wavelengths of ~45 km. These wavelengths are still too long to image magma chambers, so these shallow low velocities instead indicate a broad region of the lithosphere that must be modified to cause the reduction in velocity. The location of the shallow low-velocity anomaly is centered between earthquake swarms in the upper 30 km and the location of the Lōʻihi Seamount (Figure 2.11). We therefore propose that we are imaging evidence of shallow lithospheric modification in response to the arrival of the next volcano in the island chain.

2.6. SUMMARY

We derive a 3D model (HW13-SVJ) of the Hawaiian plume extending from the lower mantle to the surface using a multiconstraint seismic tomography method that uses the PLUME OBS data. Checkerboard resolution tests and the synthetic tests suggest that the primary features in our model are robust to 800 km depth. Our results show that under the Hawaiian hotspot a continuous low-velocity anomaly extends from the roots of the volcanoes downward into the lower mantle. The plume origin is southeast of the island chain, which is consistent with what mantle flow models predict. The geometry of this low-velocity body is consistent with a whole-mantle plume feeding the hotspot in this region. The 2%

low-velocity anomaly in the lower mantle implies a 200–250°C temperature anomaly once corrected for damping and assuming a purely thermal plume. These modeled deep features are similar to prior body wave tomography results [*Wolfe et al.*, 2009, 2011].

The addition of surface wave phase velocity constraints from earthquakes and ambient seismic noise provides additional constraints in the upper mantle, including the lithosphere and crust, which are jointly inverted with the body wave constraints. In the upper mantle, the structure of the low-velocity plume deviates substantially from the classic plume pancake model. Our model suggests the presence of two sub horizontal low-velocity layers in the upper mantle. The first is immediately below the oceanic lithosphere, as expected. The second anomaly is directly above the 410 km boundary and extends up to ~250 km depth. This secondary tomographic feature is consistent with geodynamic models of plumes with high eclogite content [*Ballmer et al.*, 2013]. They predict a low-velocity layer immediately above the 410 discontinuity produced by the accumulation of eclogite. The model also suggests a lateral heterogeneity inside this low-velocity layer that may be related to the observed geochemistry asymmetry at the surface (Chapter 3).

At more shallow, lithospheric depths, our model shows lower velocities than expected for the ~100 Ma oceanic lithosphere. Instead the velocity profiles are more similar to the Pacific lithosphere with a mantle age of 20–50 Ma. This is consistent with previous observations and interpretations of a rejuvenated lithosphere beneath the Island of Hawaiʻi [*Laske et al.*, 2011]. Finally, at the shallowest depth

(~20 km), we see a low-velocity anomaly southeast of the Island of Hawai'i that is likely indicative of the process of lithospheric modification beneath the next newly evolving island in the Hawaiian chain.

ACKNOWLEDGMENTS

REFERENCES

Abouchami, W. (2005), Lead isotopes reveal bilateral asymmetry and vertical continuity in the Hawaiian mantle plume, *Nature, 434*, 851–856.

Afonso, J. C., J. Ranalli, M. Fernàndez, W. Griffin, S. Y. O'Reilly, and U. Faul, (2010), On the Vp/Vs–Mg# correlation in mantle peridotites: Implications for the identification of thermal and compositional anomalies in the upper mantle, *Earth Planet. Sci. Lett. 289*, 606–618.

Allen, R. M., et al. (2002), Imaging the mantle beneath Iceland using integrated seismological techniques, *J. Geophys. Res.*, *107*, doi:10.1029/2001JB000595.

Allen, R. M., and J. Tromp (2005), Resolution of regional seismic models: Squeezing the Iceland anomaly, *Geophys. J. Int.*, *161*, 373–386 doi:10.1111/j.1365-246X.2005 .02600.x.

Aoki, I., and E. Takahashi, (2004). Density of MORB eclogite in the upper mantle, *Phys. Earth Planet. Int.*, *143–144*, 129–143.

Ballmer, M., G. Ito, C. Wolfe, and S. Solomon, (2013). Double-layering of a thermochemical Hawaiian plume in the upper mantle, *Earth Planet. Sci. Lett.*, *376*, 155–164, doi:10.1016/j.epsl.2013.06.022.

Cadio, C., M. D. Ballmer, I. Panet, M. Diament, and N. Ribe (2012), New constraints on the origin of the Hawaiian swell from wavelet analysis of the geoid to topography ratio, *Earth Planet. Science Lett.*, *359*, 40–54.

Cao, Q., R.D. Van der Hilst, M.V. De Hoop, and S.-H. Shim (2011), Seismic imaging of transition zone discontinuities suggests hot mantle west of Hawaii, *Science*, *332*, 1068, doi:10.1126/science.1202731.

Cheng, C., Allen, R. M., Porritt, R. W., Ballmer, M. D., 0000 Seismic constraints on a double-layered asymmetric whole-mantle plume beneath Hawaii, in: R. Carey, D. Weis, M. Poland, (Eds), *Hawaiian Volcanism: From Source to Surface*, AGU Monograph, this volume.

Cserepes, L. and D. A. Yuen (2000). On the possibility of a second kind of mantle plume, *Earth Planet. Sci. Lett. 183*, 61–71.

Dahlen, F. A., S. H. Hung, and G. Nolet (2000). Frechet kernels for finite-frequency traveltimes—I. Theory, *Geophys. J. Int*., *141*, 157–174.

Detrick, R. S. and S. T. Crough (1978). Island subsidence, hot spots, and lithospheric thinning, *J. Geophys. Res.*, *83*, 1236–1244.

Farnetani, C. G., and A. W. Hofmann (2009), Dynamics and internal structure of a lower mantle plume conduit, *Earth Planet. Sci. Lett. 282*, 314–322, doi:10.1016/j.epsl.2009.03.035.

Farnetani, C. G., and A. W. Hofmann (2010), Dynamics and internal structure of the Hawaiian plume, *Earth Planet. Sci. Lett. 295*, 231–240, doi:10.1016/j.epsl.2010.04.005.

Farnetani, C. G., A.W. Hofmann and C. Class (2012), How double volcanic chains sample geochemical anomalies from the lowermost mantle, *Earth Planet. Sci. Lett.*, *359–360*, 240–247, doi:10.1016/j.epsl.2012.09.057.

Faul, U.H. and I. Jackson (2005), The seismological signature of temperature and grain size variations in the upper mantle, *Earth Planet. Sci. Lett.*, *234*, 119–134, doi:10.1016/j.epsl.2005.02.008.

Forsyth, D. W., and A. Li (2005), Array-analysis of two-dimensional variations in surface wave velocity and azimuthal anisotropy in the presence of multipathing interference, in Seismic Earth: Array Analysis of Broadband Seismograms, Geophys. Monogr. 157, edited by A. Levander and G. Nolet, pp. 81–97, AGU, Washington, D. C.

Hammond, W. C., and E. D. Humphreys (2000), Upper mantle seismic wave velocity: Effects of realistic partial melt geometries, *J. Geophys. Res. 105*, 10,975–10,986.

Hauri, E. H., J. C. Lassiter, and D. J. DePaolo (1996), Osmium isotope systematics of drilled lavas from Mauna Loa, Hawaii, *J. Geophys. Res.*, *101*(B5), 11,793–11,806, doi:10.1029/95JB03346.

Herzberg, C., P. D. Asimow, N. Arndt, Y. L. Niu, C. M. Lesher, J. G. Fitton, M. J. Cheadle, and A. D. Saunders (2007), Temperatures in ambient mantle and plumes: constraints from basalts, picrites, and komatiites, *Geochem. Geophys. Geosyst.*, *8*, 34.

Herzberg, C., (2011), Identification of source lithology in the Hawaiian and Canary islands: Implications for origins, *J. Petrol.*, *52*, 113–146.

Huang, S., P. S. Hall, and M. G. Jackson (2011), Geochemical zoning of volcanic chains associated with Pacific hotspots, *Nature Geosci.*, *4*, 874–878.

Hung, S. H., F. A. Dahlen and G. Nolet (2000), Freć chet kernels for finite-frequency traveltimes—II. Examples, *Geophys. J. Int.*, *141*, 175–203.

Hung, S. H., Y. Shen and L.Y. Chiao (2004), Imaging seismic velocity structure beneath the Iceland hot spot: A finite frequency approach, *J. Geophys. Res.*, *109*, B08305, doi:10.1029/2003JB002889.

Jackson, I., and U. H. Faul (2010) Grainsize–sensitive viscoelastic relaxation in olivine: Towards a robust laboratory–based model for seismological application, *Phys. Earth Planet. Int.*, *183*, 151–163, doi:10.1016/j.pepi.2010.09.005.

Jordan, T. H., (1979), Mineralogies, densities, and seismic velocities of garnet lherzolites and their geophysical significance, in: The Mantle Sample: Inclusions in Kimberlites and Other Volcanic, edited by F. R. Boyd and H. O. A. Meyer, pp. 1–14, AGU, Washington, D.C.

Julia, J., C. J. Ammon, R. B. Herrmann, and A. M. Correig (2000), Joint in-version of receiver function and surface wave dispersion observations, *Geophys. J. Int.*, *143*, 99–112.

Karato, S. (1993), Importance of anelasticity in the interpretation of seismic tomography, *Geophys. Res. Lett. 20*, 1623–1626.

Karato, S. (2003), Mapping water content in the upper mantle in Inside the Subduction Factory. Geophys. Monogr.*138*, edited by J. M. Eiler, pp. 135–152, AGU, Washington, D. C.

Laske, G., J. Phipps Morgan, and J. A. Orcutt (2007), The Hawaiian SWELL pilot experiment: evidence for lithosphere rejuvenation from ocean bottom surface wave data, in Plates, Plumes and Planetary Processes, Spec. Pap. 430, edited by G. R. Foulger and D. M. Jurdy, pp. 209–233, Geol. Soci. of Am., Boulder, Colo.

Laske, G., J. A. Collins, C. J. Wolfe, S. C. Solomon, R.S. Detrick, J. A. Orcutt, D. Bercovici, and E.H. Hauri (2009), Probing the Hawaiian hot spot with new broadband ocean bottom instruments, *EOS Trans. Am. Geophys. Union.*, *90*, 362–363.

Laske, G., A. Markee, J. A. Orcutt, C. J. Wolfe, J. A. Collins, S. C. Solomon, R.S. Detrick, D. Bercovici, and E. H. Hauri (2011), Asymmetric shallow mantle structure beneath the Hawaiian Swell—Evidence from Rayleigh waves recorded by the PLUME network, *Geophys. J. Int.*, *187*, 1725–1742.

Lassiter, J. C., D. J. DePaolo and M. Tatsumoto (1996), Isotopic evolution of Mauna Kea volcano: Results from the initial phase of the Hawaiian Scientific Drilling Project, *J. Geophys. Res, 101*, 11,769–11,780.

Leahy, G. M., J. A. Collins, C. J. Wolfe, G. Laske, and S. C. Solomon (2010), Underplating of the Hawaiian Swell: Evidence from teleseismic receiver functions, *Geophys. J. Int. 183*, 313–329, doi:10.1111/j.1365-246X.2010.04720.x

Li, X., R. Kind, K. Priestley, S. Sobolev, and F. Tilmann (2000). Mapping the Hawaiian plume conduit with converted seismic waves, *Nature, 405* (2000), 938–941.

Li, X., R. Kind, X. Yuan, I. Wölbern, and W. Hanka (2004), Rejuvenation of the lithosphere by the Hawaiian plume, *Nature*, *427* (2004), 827–829.

Monnereau, M., M. Rabinowicz, and E. Arquis (1993), Mechanical erosion and reheating of the lithosphere: A numerical model for hotspot swells, *J. Geophys. Res.*, *98*, 809–823.

Morgan, W. J. (1971), Convective plumes in the lower mantle, *Nature*, v. 230, pp. 42–43.

Morgan, W. J. (1972), Deep mantle convection plumes and plate motions, Bulletin of the American Association Petroleum Geology, v. 56, pp. 203–213.

Müller, R. D., M. Sdrolias, G. Gaina, and W. R. Roest (2008), Age, spreading rates, and spreading asymmetry of the world's ocean crust. *Geochem. Geophys. Geosyst.*, *9*, Q04006, doi:10.1029/2007GC001743.

Nishimura, C.E. and D.W. Forsyth (1989). The anisotropic structure of the upper mantle in the Pacific, *Geophys. J. Int.*, *96*, 203–229.

Obrebski, M., R. M. Allen, F. Pollitz, and S.-H. Hung (2011), Lithosphere-asthenosphere interaction beneath the western United States from the joint inversion of body-wave traveltimes and surface-wave phase velocities, *Geophys. J. Int.*, *185*, 1003–1021, doi:10.1111/j.1365-246X.2011.04990.x.

Paige, C. C. and M. A. Saunders (1982), LSQR: An algorithm for sparse linear equations and sparse least squares, *TOMS*, *8*, 43–71.

Pietruszka, A. J.M.D. Norman, M. O. Garcia, J. P. Marske, and D. E. Burns (2013), Chemical heterogeneity in the Hawaiian mantle plume from the alteration and dehydration of recycled oceanic crust, *Earth Planet. Sci. Lett.*, *361*, 298–309.

Priestley, K., and F. Tilmann (1999), Shear-wave structure of the lithosphere above the Hawaiian hot spot from two-station Rayleigh wave phase velocity measurements, *Geophys. Res. Lett.*, *26*, 1493–1496.

Ribe, N. M. and U. R. Christensen (1994), Three-dimensional modeling of plume-lithosphere interaction, *J. Geophys. Res.*, *99*, 669–682.

Richards, M. A. and R. W. Griffiths (1988), Deflection of plumes by mantle shear flow: experimental results and a simple theory. *Geophys. J. Int. 94*, 367–376.

Rychert, A. C., G. Laske, N. Harmon and P. Shearer (2013). Seismic imaging of melt in a displaced Hawaiian plume, *Nature Geosci., 6*, 657–660, doi:10.1038/ngeo1878.

Schilling, J. G. (1991), Fluxes and excess temperatures of mantle plumes inferred from their interaction with migrating midocean ridges, *Nature*, *352*, 397–403.

Schimmel, M., and J. Gallart (2007), Frequency-dependent phase coherence for noise suppression in seismic array data, *J. Geophys. Res.*, *112*, B04303, doi:10.1029/2006JB004680.

Schimmel, M., E. Stutzmann, and J. Gallart (2011), Using instantaneous phase coherence for signal extraction from ambient noise data at a local to a global scale, *Geophys. J. Int.*, *184*, 494–506, doi:10.1111/j.1365-246X.2010.04861.x.

Schmerr, N., and E. Garnero (2006), Investigation of upper mantle discontinuity structure beneath the central Pacific using SS precursors, *J. Geophys. Res, 111*, doi:10.1029/2005JB004197.

Schmerr, N., E. Garnero, and A. McNamara (2010), Deep mantle plumes and convective upwelling beneath the Pacific Ocean, *Earth Planet. Sci. Lett.*, *294*,143–151.

Schutt, D. L. and C. E. Lesher (2006), Effects of melt depletion on the density and seismic velocity of garnet and spinel lherzolite, *J. Geophys. Res.*, *111*, B05401, doi:10.1029/2003JB002950.

Shen, Y., C. J. Wolfe and S. C. Solomon (2003), Seismic evidence for a mid-mantle discontinuity beneath Hawaii and Iceland, *Earth Planet. Sci. Lett.*, *214*, 143–151.

Sobolev, A. V., A. W. Hofmann, S. V. Sobolev, and I. K. Nikogosian (2005), An olivine-free mantle source for Hawaiian shield basalts, *Nature*, *434*, 590–597.

Steinberger, B., and R. J. O'Connell (1998), Advection of plumes in mantle flow: implications on hotspot motion, mantle viscosity and plume distribution, *Geophys. J. Int.*, *132*, 412–434.

Steinberger, B., R. Sutherland and R. J. O'Connell (2004), Prediction of Emperor-Hawaii seamount locations from a revised model of plate motion and mantle flow, *Nature, 430*, 167–173.

Tilmann, F. J., H. M. Benz, K. F. Priestley and P.G. Okubo (2001). P-wave velocity structure of the uppermost mantle beneath Hawaii from traveltime tomography, *Geophys. J. Int.*, *146*, 594–606.

VanDecar, J. C. and R. S. Crosson (1990), Determination of teleseismic relative phase arrival times using multi-channel cross-correlation and least squares, *Bull. seism. Soc. Am.*, *80*, 150–169.

Von Herzen, R. P., M. J. Cordery, R. S. Detrick, and C. Fang (1989), Heat flow and the thermal origin of hot spot swells: The Hawaiian Swell revisited, *J. Geophys. Res.*, *94*, 13,783–13,799.

Weis, D., M. O. Garcia, J. M. Rhodes, M. Jellinek, J.S. Scoates (2011), Role of the deep mantle in generating the compositional asymmetry of the Hawaiian mantle plume, *Nature Geosci. 4*, 831–838.

Wessel, P. and W. H. F. Smith (1998), New, improved version of the Generic Mapping Tools released, *EOS Trans. AGU, 79*, 579.

Wölbern, I., A. Jacob, T. Blake, R. Kind, X. Li (2006), Deep origin of the Hawaiian tilted plume conduit derived from receiver functions, *Geophys. J. Int., 166*, 767–781.

Wolfe, C. J., S. C. Solomon, G. Laske, J. A. Collins, R. S. Detrick, J. A. Orcutt, D. Bercovici, and E. H. Hauri (2009), Mantle shear-wave velocity structure beneath the Hawaiian hot spot, *Science*, *326*, 1388–1390, doi:10.1126/science.1180165.

Wolfe, C. J., S. C. Solomon, G. Laske, J. A. Collins, R. S. Detrick, J. A. Orcutt, D. Bercovici, and E. H. Hauri (2011), Mantle P-wave velocity structure beneath the Hawaiian hot spot, *Earth planet. Sci. Lett.*, *303*, 267–280.

Woods, M. T. and E.A. Okal (1996), Rayleigh-wave dispersion along the Hawaiian Swell: A test of lithospheric thinning by thermal rejuvenation at a hotspot, *Geophys. J. Int.*, *125*, 325–339.

Yang, Y., and D. W. Forsyth (2006a), Regional tomographic inversion of amplitude and phase of Rayleigh waves with 2-D sensitivity kernels, *Geophys. J. Int.*, *166*, 1148–1160.

Yang, Y., and D. W. Forsyth (2006b), Rayleigh wave phase velocities, small-scale convection and azimuthal anisotropy beneath southern California, *J. Geophys. Res.*, *111*, B07306, doi:10.1029/2005JB004180.

Yang, Y., A. Li, and M. H. Ritzwoller (2008), Crustal and uppermost mantle structure in southern Africa revealed from ambient noise and teleseismic tomography, *Geophys. J. Int.*, *174*(1), 235–248, doi:10.1111/j.1365-246X.2008.03779.x.